J. Fluid Mech. (1994), vol. 259, pp. 1–24

The structure of a supersonic turbulent boundary layer subjected to concave surface curvature

By JOHN F. DONOVAN[1], ERIC F. SPINA[2] AND ALEXANDER J. SMITS[3]
[1] McDonnell Douglas Aerospace, St Louis, MO 63166, USA
[2] Syracuse University, Mechanical and Aerospace Engineering Department, Syracuse, NY, USA
[3] Princeton University Gas Dynamics Laboratory Princeton, NJ 08544, USA

(Received 22 May 1992 and in revised form 6 July 1993)

This paper reports an experimental investigation of the instantaneous structure of a supersonic turbulent boundary layer ($M = 2.86$, $Re_\theta = 82000$) over a short region of longitudinal concave surface curvature. The radius of curvature was 12 initial boundary-layer thicknesses and the turning angle was 16°. Severe distortion of the boundary layer occurred, as evidenced by an alteration of the mean velocity profiles and an increase in wall shear stress of 125%. The large-scale organized motions in the boundary layer were significantly altered as illustrated by changes in the character of the mass flux 'fronts' (large gradients in the fluctuating streamwise mass flux).

1. Introduction

In this paper we report an experimental study of the response of the large-scale motions in a supersonic turbulent boundary layer to a relatively short region of strong concave surface curvature. The boundary layer upstream of the perturbation had a free-stream Mach number of 2.86, and a Reynolds number based on momentum thickness of 82000. The ratio of the initial boundary-layer thickness, δ_0, to the radius of curvature, R, was $\delta_0/R = 0.08$, and the turning angle was $\theta = 16°$. The compression fan did not focus into a shock wave until clear of the boundary layer, and thus the turning and compression were continuous.

Our primary interest in studying this flow was the combined effects of all the extra strain rates resulting from concave surface curvature in supersonic flow. Within the curved region, and for a short distance downstream, the boundary layer experiences the combined effects of significant extra strain rates associated with streamline curvature, ($\partial V/\partial x$), pressure gradient, ($\partial p/\partial x$ and $\partial p/\partial y$), and bulk compression ($\nabla \cdot V$). These perturbations are examples of what Bradshaw (1973) called 'extra' strain rates – strain rates additional to the main shear $\partial U/\partial y$. Adverse pressure gradient, bulk compression, and concave streamline curvature all act to increase turbulence levels separately, but little is known regarding their simultaneous action. For example, concave surface curvature in subsonic boundary layers appears to generate Taylor–Görtler-type vortices, even when the flow is turbulent (Bradshaw 1973). The absence of longitudinal roll cells in supersonic, concavely curved flows was noted by Sturek & Danberg (1972*a*, *b*), Laderman (1980), and Jayaram, Taylor & Smits (1987), who suggested that the nonlinear interaction of concave curvature (which tends to amplify longitudinal vorticity) and compression (which tends to amplify spanwise vorticity) may act to prevent the formation of roll cells. It is always possible that unsteady Taylor–Görtler roll cells existed in these flows, but they would not have been detected by the measurement techniques used.

Similar concave–curvature flows were studied by, for example, McLafferty & Barber (1962), Thomann (1968), Hoydysh & Zakkay (1969), Sturek & Danberg (1971), Laderman (1980), and Chou & Childs (1983), but their focus was confined to the behaviour of the mean flow. Detailed turbulence measurements in such flows were first reported by Jayaram *et al.* (1987). In that work the effects of two different short regions of concave surface curvature were investigated, one with $\delta_0/R = 0.1$ and one with $\delta_0/R = 0.02$, both having a turning angle of 8°. Downstream of the curved region the flow relaxed on a plane wall. As in the present study, the upstream freestream Mach number was 2.86 with $Re_\theta = 82000$.

In an effort to separate the effects of curvature and pressure gradient, Fernando & Smits (1990) and Smith (1993) examined the effects of two different adverse pressure gradients on flat-plate boundary layers with the same initial conditions as in the present study. The pressure distribution of Fernando & Smits matched that of the $\delta_0/R = 0.02$ flow studied by Jayaram *et al.*, while that of Smith (1993) matched the pressure distribution of the $\delta_0/R = 0.08$ case reported here. The skin friction increased and the turbulence was amplified strongly in both adverse-pressure gradient flat-plate studies. For example, Fernando & Smits ($p_2/p_1 = 1.9$) found a maximum amplification in $\overline{\rho u'^2}$ of about 2.8, whereas Smith ($p_2/p_1 = 3.2$) found a maximum amplification of about 5.

The previous studies of extra strain rates in supersonic boundary layers have led to some uncertainty about the response of the mean flow and the Reynolds stresses to concave curvature and bulk compression. The current work is primarily concerned with the effects of a short region of strong concave surface curvature on the large-scale turbulence structure, and how these changes relate to the behaviour of the Reynolds stresses.

2. The experiment

All experimental work was performed in the Princeton University high-Reynolds-number 200 mm × 200 mm supersonic blowdown wind tunnel. The upstream conditions were identical to those used by Jayaram *et al.* (1987), Fernando & Smits (1990), Spina, Donovan & Smits (1991 *a*, *b*) and Smith (1993), and the initial boundary-layer parameters are given in table 1. The experimental procedure followed that of Spina *et al.* (1991 *a*) closely, and further details may be found there. Briefly, the model was installed on the tunnel floor 1149 mm from the nozzle exit. The radius of curvature, R, was 350 mm and the turning angle, θ, was 16°. This case corresponds to Model IV, in the terminology of Fernholz *et al.* (1989), where the data are given in detail (catalogue numbers 8401 for the mean flow, and 8702T for the turbulence measurements). The model did not span the entire width of the tunnel to allow for the passage of the sidewall boundary layers, and fences were placed on the model sides to improve the two-dimensionality of the flow further. A sketch of the model can be seen in figure 1. The origin of the orthogonal coordinate system is on the centreline of the wall at the start of curvature, and x is the streamwise distance along the model surface, y is the coordinate normal to the wall, and z is the spanwise coordinate. The curved region ends at $x = 98$ mm ($3.5\ \delta_0$).

Mean-flow data include Preston-probe surveys, static- and Pitot-pressure surveys, wall pressures, and kerosene-lamp black surface flow studies (Settles & Tena 1982). The local skin friction coefficient was found using two different techniques: Preston-probe measurements reduced according to the correlation proposed by Bradshaw & Unsworth (1974*a*), and the method of Clauser (1954) applied to Van Driest-transformed velocity profiles (Van Driest 1951).

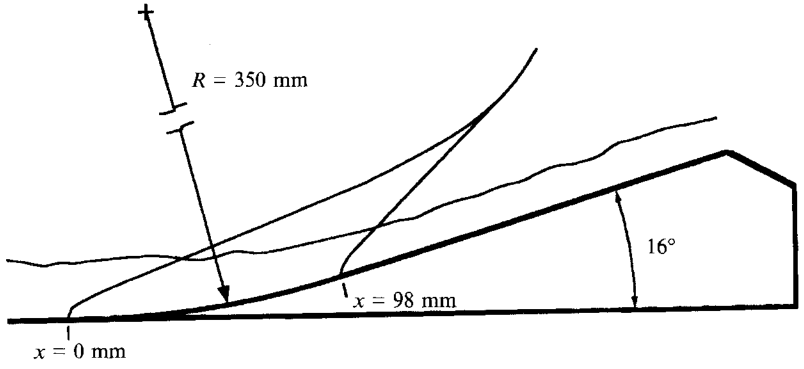

FIGURE 1. Side view of the model used in the present investigation with a sketch of the flow field; x values at the beginning and end of curvature are indicated.

Re_{ref}/m	6.3×10^7 m^{-1}
$M_{e,\,ref}$	2.86
$p_{w,\,ref}$	0.23×10^5 N/m^2
P_0	6.9×10^5 N/m^2
T_0	270 K
T_w/T_0	1.04
$U_{e,\,ref}$	580 m/s
$\rho_{e,\,ref}$	0.789 kg/m^3
δ_{ref}	28 mm
δ^*_{ref}	7.2 mm
θ_{ref}	1.3 mm
Re_θ	82000

TABLE 1. Nominal incoming flow conditions and stagnation conditions

Experimental data were obtained using single-, double-, and crossed-wire anemometry as well as high-speed schlieren photography. Conditional sampling, cross-correlation, and cross-spectral techniques were used to interpret the hot-wire signals. Hot-wire measurements were taken using DISA 55M10 constant-temperature anemometers according to the techniques developed by Smits, Hayakawa & Muck (1983) for the normal wire, and Donovan & Spina (1992) for the crossed wire. Single normal wires were used to measure $(\rho u)'$, and crossed wires were used to measure $(\rho u)'$ and the transverse velocity component v' simultaneously. Total-temperature fluctuations were not measured independently, so the root-mean-square form of Morkovin's (1962) strong Reynolds analogy (SRA) was used to derive $\bar{\rho}\overline{u'^2}$, $\bar{\rho}\overline{v'^2}$, and $\bar{\rho}\overline{u'v'}$ (which we will refer to as the Reynolds streamwise, normal, and shear stresses, respectively). To apply the SRA in this flow, it was assumed that the temperature/velocity correlation was constant and equal to -0.8 (Gaviglio 1987). The density was determined from the temperature by assuming the pressure fluctuations were negligible, which appears to be a reasonable assumption at this Mach number (see Spina *et al.* 1991*a* for a more complete discussion, especially regarding the nature of the Reynolds shear stress in a compressible flow). Recent measurements by Smith & Smits (1993) of the instantaneous velocity and density in strongly perturbed flows lend support for the use of the strong Reynolds analogy at this Mach number.

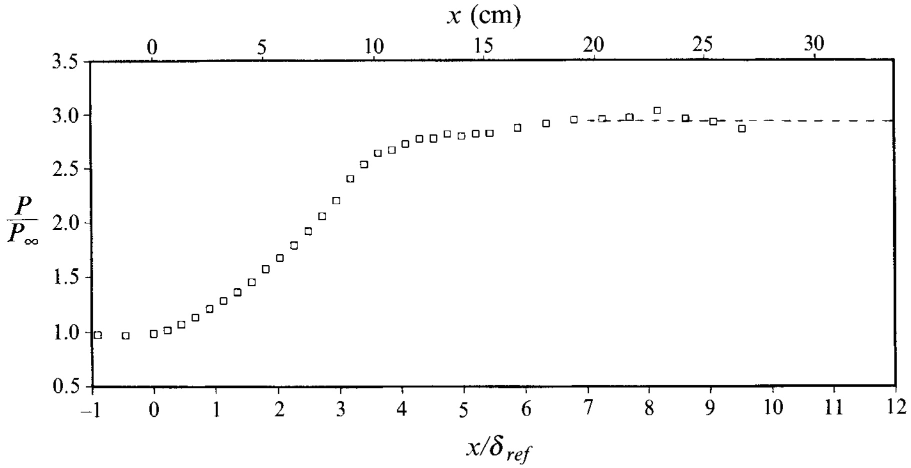

FIGURE 2. Streamwise variation of wall static pressure. The dashed line indicates the pressure calculated assuming inviscid turning.

3. Mean flow results

As expected from previous work (see §1), no evidence of steady Taylor–Görtler vortices was found, either in the surface flow patterns, the spanwise wall-pressure distributions, or the spanwise skin friction. In fact, the spanwise distributions of the wall pressure and the skin friction showed less than ±1% and ±3.5% variation, respectively, across the central 50 mm of the model. This variation was considered acceptably two-dimensional.

Figure 2 shows the streamwise wall-pressure distribution at the centreline. The pressure rise is smooth and extends slightly downstream of the end of curvature. The calculated pressure based upon isentropic turning was found to be in excellent agreement with the measured pressure at the farthest downstream station, with only a slight overshoot. A similar overshoot was observed by Jayaram *et al.* (1987) in their study of the flow with 8° of turning. The tunnel was checked for disturbances which might cause this behaviour, such as a compression wave originating at the tunnel ceiling, but none were located and the overshoot was accepted as part of the natural flow response. The free-stream flow response is characterized by a decrease in Mach number from 2.86 to 2.10, an increase in density by a factor of 2.1, and a decrease in velocity by a factor of 0.88.

The wall shear stress, normalized by the upstream free-stream density and velocity, is plotted in figure 3. The values of $C_{f,ref}$ determined by two different methods agree to within about ±10% throughout the measurement region. Smith *et al.* (1992) indicate that the Preston tube results analysed using the Bradshaw & Unsworth (1974*a*) calibration are the most reliable in perturbed flows. The absolute value of the wall shear stress increases by about 125%. If the local free-stream conditions were used to non-dimensionalize τ_w, the increase in C_f would still be about 77% (however, this non-dimensionalization is only valid where $\partial p/\partial x$ is small). The increase in shear stress is counter to that observed in subsonic flows, where an adverse pressure gradient decreases the wall shear stress. This counter-intuitive behaviour occurs because the density increases more than the velocity decreases. As a result, the boundary-layer thickness decreases and the velocity gradient at the wall increases. The wall stress continues to increase well after the removal of curvature and even after the pressure

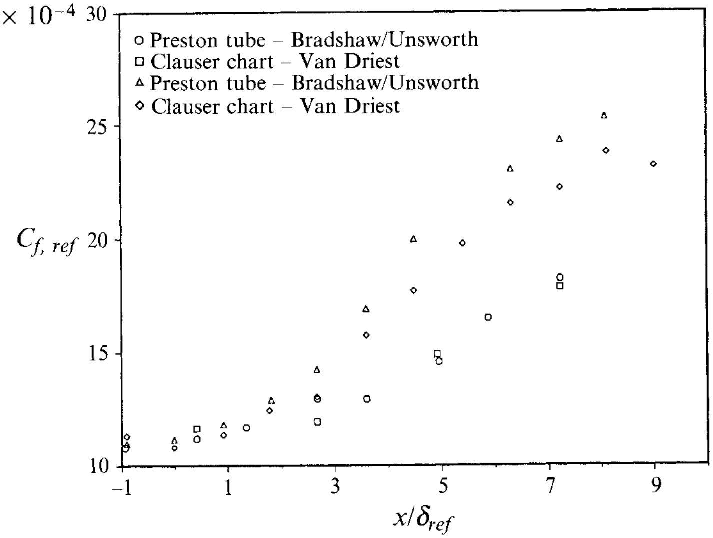

FIGURE 3. Streamwise wall stress variation for the curved and flat plate flows based on two reduction methods. ○, □, flat plate flow (from Smith 1993); △, ◇, present investigation.

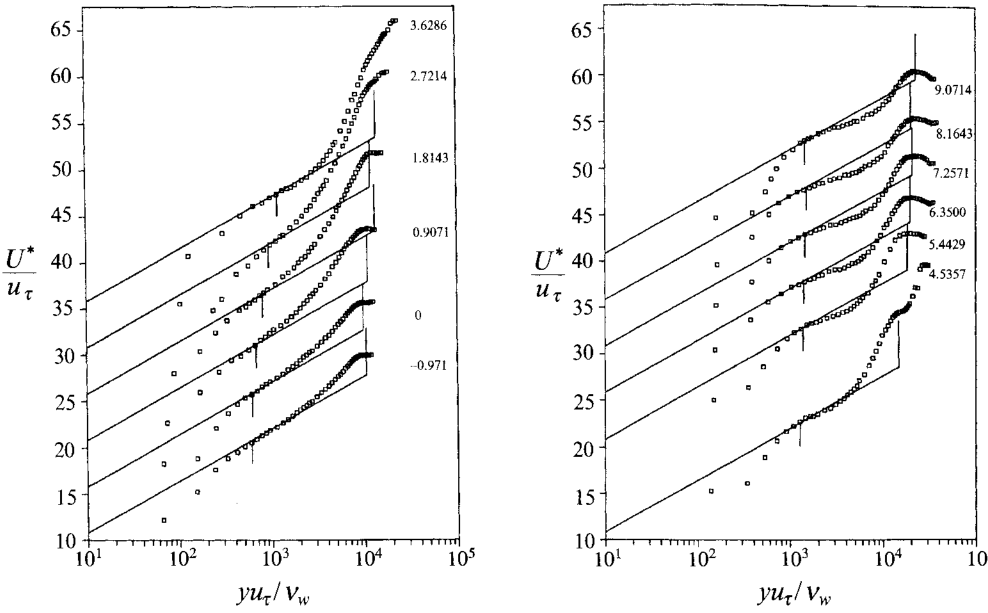

FIGURE 4. Van Driest transformed mean velocity profiles. The vertical bar near 1000 indicates the Preston probe diameter and the vertical bar near 10000 indicates the boundary-layer edge. The x/δ_{ref} values are indicated to the right of the profiles.

gradient ends. A similar behaviour was noted by Smith (1993) in his parallel study of an equivalent adverse pressure gradient on a flat-plate boundary layer. There, the wall stresses increased by about 60% (see figure 3).

The Van Driest-transformed velocity profiles are show in figure 4 in log–law coordinates. The undisturbed boundary-layer profile exhibits an extensive logarithmic

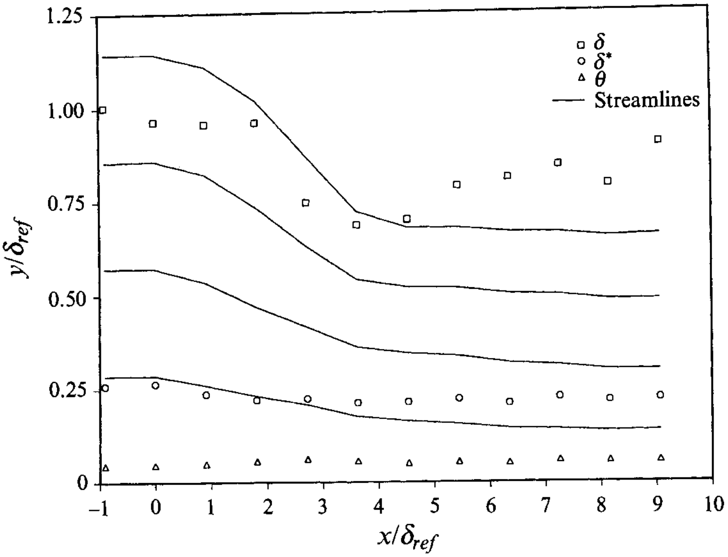

FIGURE 5. Streamwise variation of the boundary-layer thickness, displacement thickness, and momentum thickness. Mean streamlines are also plotted.

region.† By the end of the curved region ($x/\delta_{ref} = 3.5$) the profile begins to dip below the logarithmic law near the point where $y^+ = 2000$. This dip grows in size and extends farther into the logarithmic region with increasing downstream distance. A dip in the logarithmic region is a common feature of flows with concave surface curvature, and it may indicate that the lengthscales of the turbulent motions increase faster with distance from the wall than in the unperturbed boundary layer (Bradshaw 1973; Smits *et al.* 1979*b*; Jayaram *et al.* 1987). The maximum extent of the dip below the logarithmic law in the current curved-wall flow is similar to that observed by Jayaram *et al.* in a case with only 8° of turning and $\delta_0/R = 0.02$ (Model II in the terminology of Fernholz *et al.* 1989). The dip does not become significant until after the curved region ends in both flows, suggesting that the inner region of the boundary layer either is exhibiting a delayed response to the curvature or is responding relatively quickly to the removal of curvature.

The two adverse-pressure gradient/flat-plate studies that were done in parallel to this study and to the curved-wall experiments of Jayaram *et al.* provide some insight into the log–law dip. The weaker flat-plate case (Fernando & Smits, matching the curved wall of Jayaram *et al.*) exhibits a dip, but $6.9\delta_0$ farther downstream than in the matching curved flow. This delay may be due to the weaker normal pressure gradients in the flat-plate case, or the lack of significant streamline curvature, or a combination of both factors. The appearance of similar dips in subsonic curved-wall flows (see Smits *et al.* 1979*b*), where the predominant effect is streamline curvature, would seem to indicate that normal pressure gradients may not cause the dip. Curiously, the stronger adverse-pressure gradient/flat-plate boundary layer (Smith 1993, matching the current experiment) does not exhibit a dip, but this study has a more limited streamwise extent than the other considered here.

The integral parameters are shown in figure 5. Displacement and momentum thicknesses were calculated using the method proposed by Fernholz & Finley (1980)

---

† The discrepancies near the wall are caused by the 0.2 mm uncertainty in the y-position: wall interference effects were important for only the first one or two points within a profile, and they were routinely discarded.

which takes account of the inviscid variations in velocity owing to the curvature and compression of the flowfield. The boundary-layer thickness was defined as the point where the difference between the total pressure and the wall pressure reached 99% of its free-stream value. This method of finding δ was found to be more consistent than the usual definition in terms of the mass flux or velocity. For reference, mean streamlines are also shown in figure 5. The outer streamline crosses the boundary-layer edge, indicating that non-turbulent fluid is being entrained by the boundary layer even in the region of adverse pressure gradient. Similar streamline behaviour was noted by Jayaram *et al.* in Model II, and by Fernando & Smits (1990) and Smith (1993) in the adverse-pressure gradient/flat-plate flows.

In summary, the incoming flow is severely distorted, as evidenced by the deviation of the mean velocity profiles and the large increase in wall friction. The flat-plate flow that matches the pressure distribution of the curved flow exhibits a smaller distortion of these quantities, and the differences can be attributed to the curvature effects, although the normal pressure gradient may also play a role.

4. Mean turbulence behaviour

Reynolds streamwise stress profiles are given in figure 6. The levels increase considerably through the perturbation: for instance, at $y/\delta = 0.4$ the stress increases by a maximum factor of 6.8. Although not apparent in figure 6, the first signs of amplification occur at points close to the wall, where the timescales are small. By the last streamwise station, the relaxation process has begun at points in the boundary layer below 0.6δ, but the fluctuations are still growing in the outer 20% of the boundary layer. This clearly illustrates the variation in response times across the layer. In strongly perturbed supersonic boundary layers (e.g. Hayakawa, Smits & Bogdonoff 1984; Smits & Muck 1987; Jayaram *et al.* 1987), changes in the level of the local mass-flux fluctuations, $\overline{(\rho u)'^2}/\overline{\rho U}^2$, are always much smaller than changes in the Reynolds stresses. In the present study, for example, the maximum increase in the local mass-flux fluctuations is only about 60%. These differences between mass-flux and velocity fluctuations are primarily caused by the increase in mean density, which increases by a factor of 2.1 at $y/\delta = 0.4$.

As the boundary layer exits the curved region, the angular momentum, $\rho(\partial U/\partial y)$, develops a maximum away from the wall. In a laminar boundary layer, a generalized inflexion point can make the layer unstable, at least at Mach numbers less than about 1.7 (Morkovin 1992). In the present case, the inflexion point is first seen at $x = 4.54\delta_0$, where it is located at about $y = 0.2\delta$. Downstream, it becomes more exaggerated, and its position moves slowly away from the wall so that at $x = 8.16\delta_0$ it is at about $y = 0.3\delta$. The Mach numbers at these locations are approximately 1.4 and 1.6, respectively, and it is possible that the unstable angular momentum profile contributes to the elevated levels of turbulence seen in this region of the flow.

It should also be noted that the streamwise Reynolds stress undergoes a greater amplification in the curved flow than in the corresponding adverse-pressure-gradient flow. The peak amplification factor here is about 8, compared with about 5 for the adverse-pressure-gradient flow studied by Smith (1993). Similarly, the peak amplification in Model II is a factor of 4.4, whereas the matched adverse-pressure-gradient flow studied by Fernando & Smits (1990) had an amplification factor of 2.8 at the same location. These differences are not surprising, considering the additional extra strain rates present in the curved-wall cases relative to the flat-plate adverse-pressure-gradient flows.

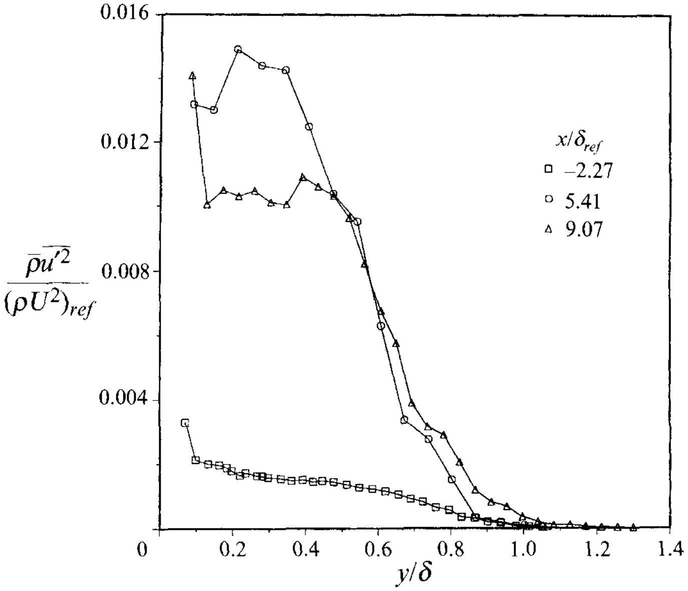

FIGURE 6. Streamwise variation of Reynolds streamwise stress profiles.

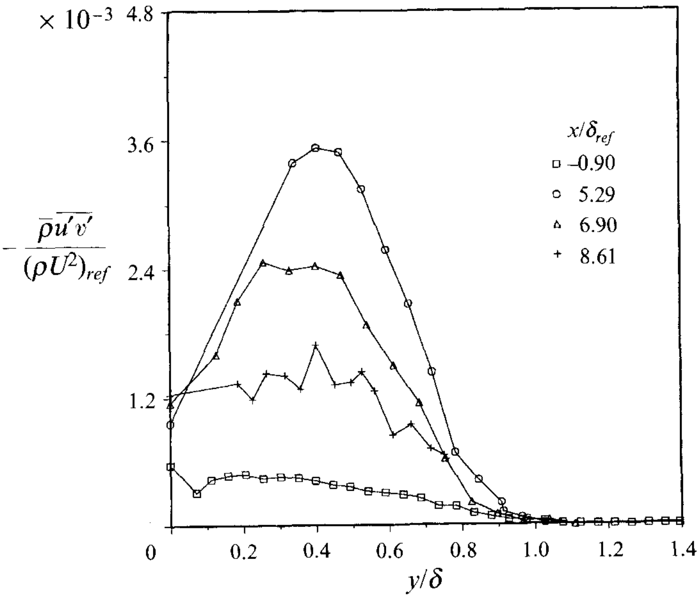

FIGURE 7. Streamwise variation of Reynolds shear stress profiles. The values plotted at $y = 0$ correspond to $\frac{1}{2}C_{f,ref}$.

Reynolds shear stress distributions are shown in figure 7. Note that near the wall ($y/\delta = 0.2$), the Mach number normal to the crossed wires can become transonic, and data below this height should be treated with caution. The first two points at $x = 5.29\delta_0$ and $6.9\delta_0$ are probably in error because of this effect. Elsewhere in the profile the uncertainty in the data is probably within ±20% (Donovan & Spina 1992). Amplification of the shear stress is largest at $y/\delta = 0.4$, where the stress has increased

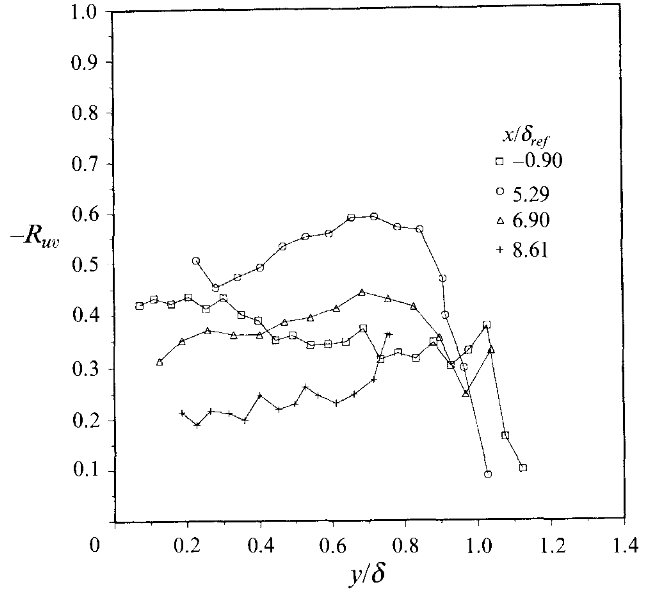

FIGURE 8. Streamwise variation of correlation coefficient R_{uv}.

by a factor of 5.3. While the amplification is not constant across the layer, (in contrast to the streamwise Reynolds stress behaviour) it is amplified across the entire height of the boundary layer. The shear stress relaxes significantly faster than the streamwise stress. The correlation coefficient $R_{uv} = -\overline{u'v'}/u_{rms}v_{rms}$ (shown in figure 8) increased by more than 60%, and the amplification was strongest in the outer part of the layer where the effects of extra strain rates are largest ($y/\delta \geqslant 0.4$).

The normal component of the Reynolds stress, $\overline{\rho v'^2}$, is shown in figure 9. A significant amplification is clearly indicated, by a factor of 6.0 at $y/\delta = 0.4$. Somewhat surprisingly, profiles of the ratio of the streamwise to normal fluctuating velocities (the anisotropy ratio) showed little change through the distortion (as a function of y/δ, u_{rms}/v_{rms} falls from about 3.5 near the wall to a value close to zero at $y \approx \delta$, see Donovan 1989 for details). Similar behaviour was observed by Fernando & Smits (1990). It should be noted that in subsonic flows the anisotropy parameter typically decreases from a maximum value of 2 near the wall to about 1.5 at $y = 1.0\delta$ (see, for example, Alving 1988). The fact that at a given location in the boundary layer the anisotropy ratio remains roughly constant, whereas R_{uv} changes by up to 60%, suggests that the organized motions have been altered significantly.

Differences between the normalized upstream and perturbed-flow spectra are not large at any location. The strongest effects occur near the wall, where the energy shifts to lower frequencies, indicating the same increase in lengthscales as noted by Jayaram *et al.* (1987) and Fernando & Smits (1990). In the present case, at $y/\delta = 0.2$ the peak shifts from about 11.5 kHz to 9.4 kHz, and the shift decreases with increasing distance from the wall (see Donovan 1989 for details).

Probability density functions for the streamwise fluctuating mass flux showed significant changes through the interaction, especially in the outer part of the boundary layer where the extra strain rates are large relative to $\partial U/\partial y$. Since the density/velocity correlation is close to one in this flow (see Smith 1993), the statistics of the fluctuations in mass flux, velocity, and density should be very similar. The skewness (third moment) of the streamwise fluctuating mass flux was reduced significantly, and the flatness

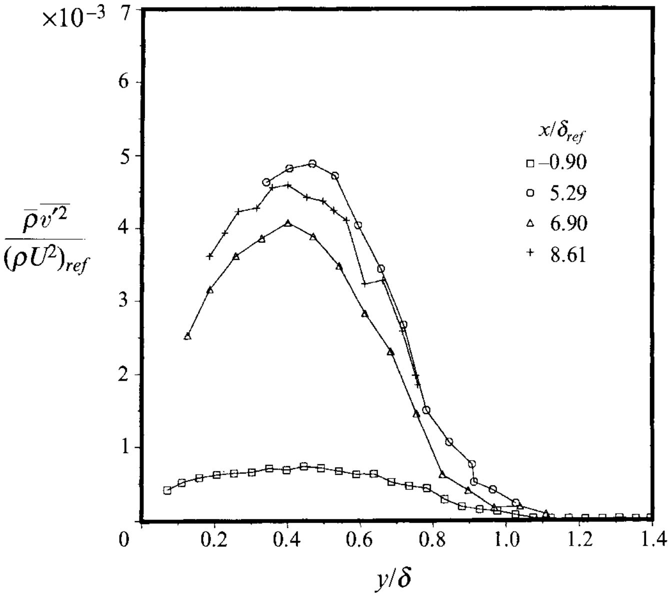

FIGURE 9. Streamwise variation of the Reynolds normal stress profiles.

(fourth moment) was increased significantly by the extra strain rates. However, the shapes of the flatness and skewness profiles were almost unchanged, and by reducing the effective boundary-layer thickness the data could almost be collapsed (see Donovan 1989 for details). This may indicate that the organized motions remain similar, but that they have been redistributed throughout the boundary layer. It may also indicate that the 99% total pressure criterion is not a good way to determine the edge of the boundary layer in a perturbed flow. Bradshaw & Unsworth (1974*b*) suggest defining the edge of the boundary layer as the point in the flow where the Reynolds shear stress falls to 5% of its peak value. This definition would reduce the boundary-layer thickness, yielding much closer agreement between the curves of skewness and flatness obtained at different streamwise locations.

5. Conditionally sampled results

VITA conditional sampling, developed by Blackwelder & Kaplan (1976), was used extensively by Spina & Smits (1987) and Spina *et al.* (1991*a*) to characterize the large-scale structure of the incoming, undisturbed boundary layer. They showed that the VITA technique detects steep streamwise mass-flux gradients in compressible boundary layers, and that large positive mass-flux gradients are significantly more numerous than large negative mass-flux gradients. The very strong positive ρu gradients detected with VITA extend over most of the boundary-layer thickness, and it was suggested that most of these events correspond to the upstream edges of large-scale turbulent bulges.

The VITA technique was also used here to study the structure of the perturbed boundary layer. When applying VITA, the threshold level and 'decision' time need to be specified. In strongly perturbed flows, it is not clear whether these parameters should be based on local conditions or on upstream conditions. After some study, the decision time, TU_{ref}/δ_0, and the threshold, k (the ratio between the short-time variance and the long-time variance), were set at constant values, with $TU_{ref}/\delta_0 = 0.27$ and $k = 1.0$.

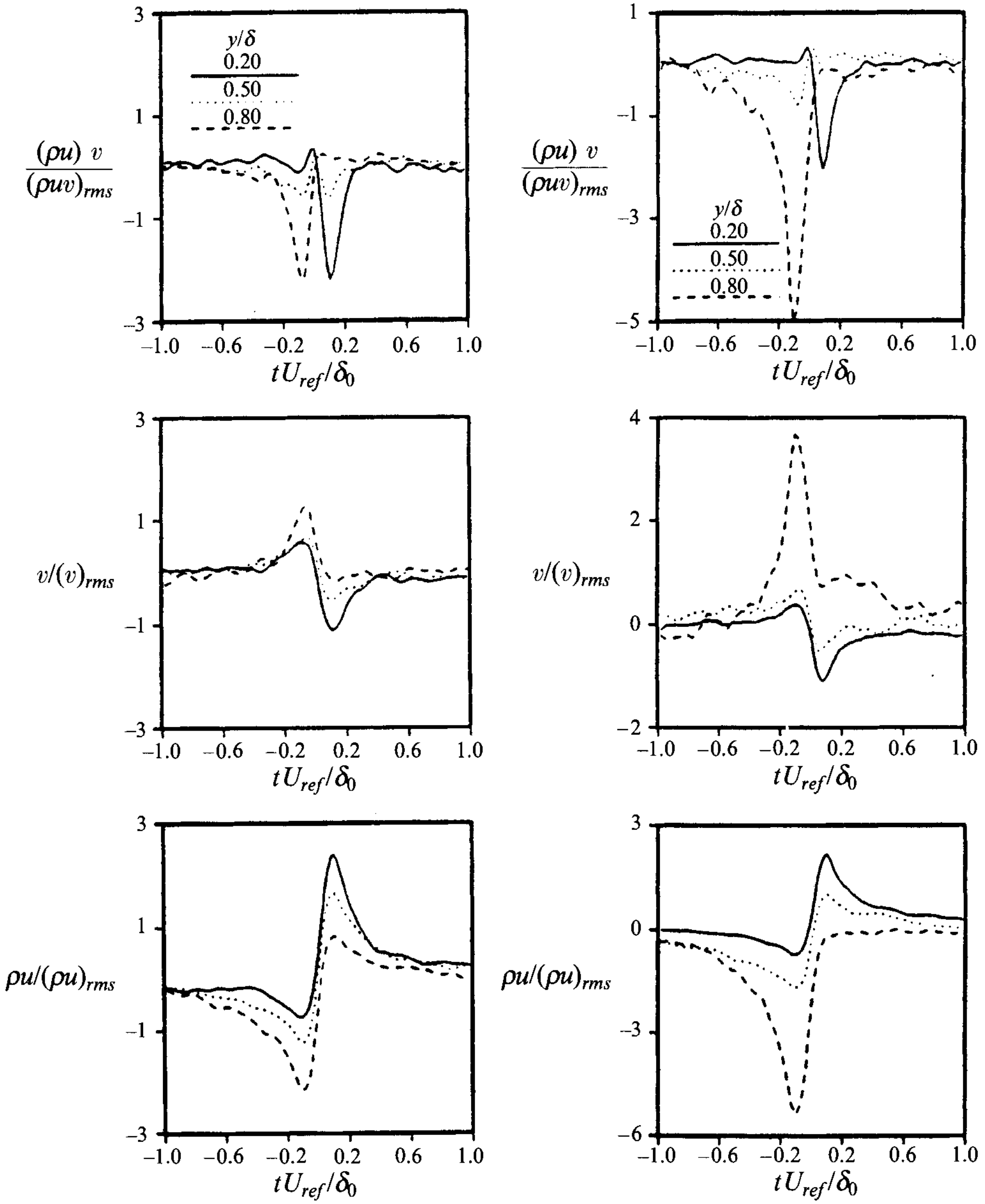

FIGURE 10. Ensemble-averaged signatures based on the VITA technique for positive events in the upstream boundary layer (left) and at $x/\delta_0 = 5.4$ (right) at three locations in each boundary layer.

Although the number of events, and to some extent the character of the deduced events, are a function of the decision time and threshold, the trends reported here were independent of the particular values chosen.

Crossed-wire measurements can be used to determine the behaviour of the streamwise mass flux, the normal velocity, and their product during passage of the strong mass-flux fronts by using the short-time variance of $(\rho u)'$ as the detection signal. Note that, according to the strong Reynolds analogy (Morkovin 1962), the product $(\rho u)' v'$ is proportional to the instantaneous contribution to the Reynolds shear stress, $\rho(u'v')$. Since a strong correspondence has been shown to exist between strong streamwise mass-flux gradients and large-scale turbulent motions in supersonic flow (Spina *et al.* 1991 *a*), we expect that the signals deduced using VITA reveal information about the flow kinematics in and around the large-scale structures.

Ensemble-averaged positive events at three locations are shown in figure 10 for a streamwise location of $5.4\delta_0$. The character of the $(\rho u)'$ signatures at a given location in the boundary layer remains virtually the same through the perturbation, an encouraging observation from a turbulence modelling point of view. However, the magnitude of the signatures is increased through the perturbation. This amplification is largest near the edge of the boundary layer (e.g. $y/\delta = 0.8$) where extra strain rates exert the strongest influence. However, fewer sharp $(\rho u)'$ gradients were found in the strongly perturbed flow, indicating that the amplification affects the detected mass-flux gradient structures more than the other turbulent motions. Although not evident in figure 10, there is a decrease in timescale of the signatures compared to those in the unperturbed flow, implying a decrease in the streamwise lengthscale. This decrease in lengthscale is consistent with the effects of bulk compression which act to reduce the streamwise and normal dimensions of a fluid element. However, the streamwise reduction is quite small in comparison to the normal reduction and is in contrast to the increased low-frequency content of $(\rho u)'$ noted in §4.

6. Two-point correlation results

Two-point measurements of the streamwise mass flux were made using vertically and horizontally separated normal hot wires to obtain spatial information about the large-scale motions.

6.1. *Convection velocity*

The streamwise-separated normal hot-wire measurements were used to obtain mean and instantaneous convection velocities. The convection velocities are of interest for two reasons. First, to determine the ensemble-averaged structure of the large-scale motions the observer needs to move at the convection velocity. Secondly, the difference between the convection velocity and the local mean velocity is some measure of the intensity of the large-scale motions, and has implications for the degree of intermittency.

Measurements of the convection velocity in the upstream boundary layer were recently presented by Spina *et al.* (1991 *b*). The broadband convection velocity was obtained from a cross-correlation between signals from two streamwise-separated normal hot wires, and the convection velocity of individual large-scale motions was obtained from the raw signals using two-point VITA conditional sampling. The latter technique is described in detail by Spina & Smits (1987) and Spina *et al.* (1991 *a*). Briefly, the method searches for highly correlated, energetic events occurring in both signals, and the time delay between the events is then used to define the convection velocity associated with the passage of that particular motion.

The same probes and data reduction techniques as in Spina *et al.* (1991 *a*) were used in the study of the flow over Model IV, with wire separations ranging from $0.11\delta_{ref}$ to $0.18\delta_{ref}$. Since the wires are arranged one behind the other in the streamwise direction, interference between the two wires is obviously a concern in the interpretation of the measurements. However, the spectra and r.m.s. mass-flux profiles obtained from the second wire were identical to those from the upstream wire, and it was concluded that the presence of the first wire did not significantly affect the scales of interest.

The broadband convection velocity data are shown in figure 11. The discrete jumps in velocity are due to the discretization of the timescale: the temporal resolution is one

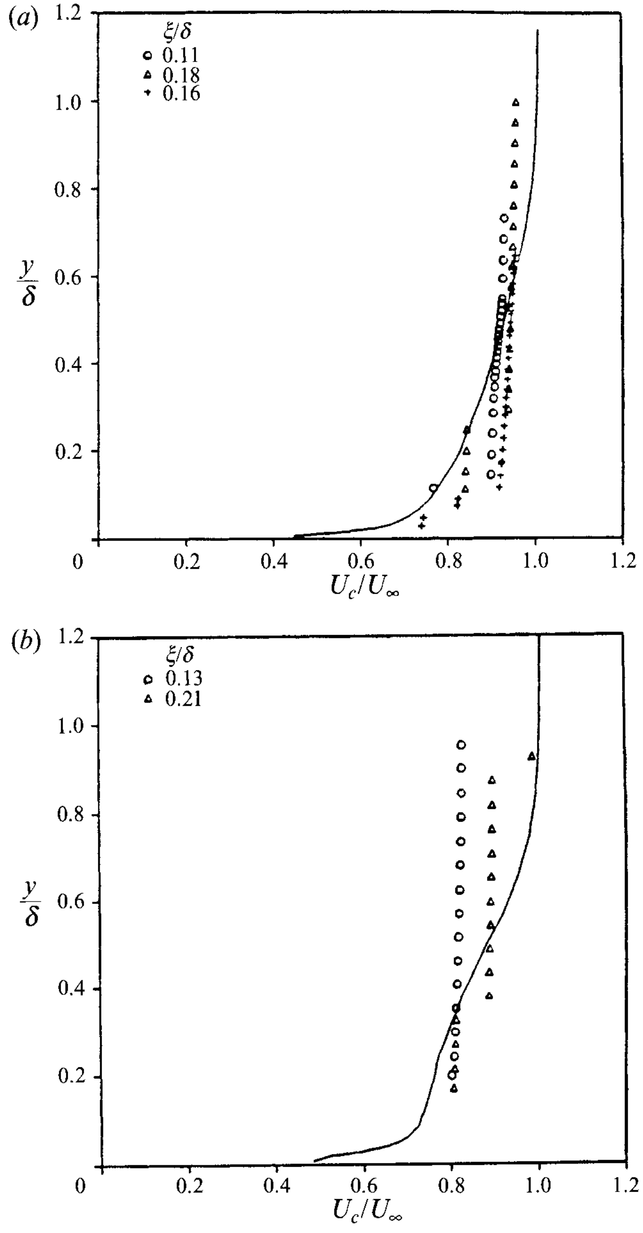

FIGURE 11. Convection velocities found using several streamwise separations (*a*) in the upstream boundary layer and (*b*) at $x/\delta_0 = 5.4$. The mean velocity profiles are included for comparison.

microsecond, equivalent to an uncertainty of about 11 % in the convection velocity in the middle of the layer. Whereas the convection velocity in the upstream boundary layer is about $0.9U_e$ throughout much of the layer (Spina *et al.* 1991*b*), the convection velocity through the perturbed flow is consistently lower. Despite the uncertainty in estimating the time delay, it appears that the convection velocity is reduced to about $0.85U_e$.

The average value of the instantaneous convection velocity as determined by the VITA technique is shown in figure 12. Since the discretization error is random,

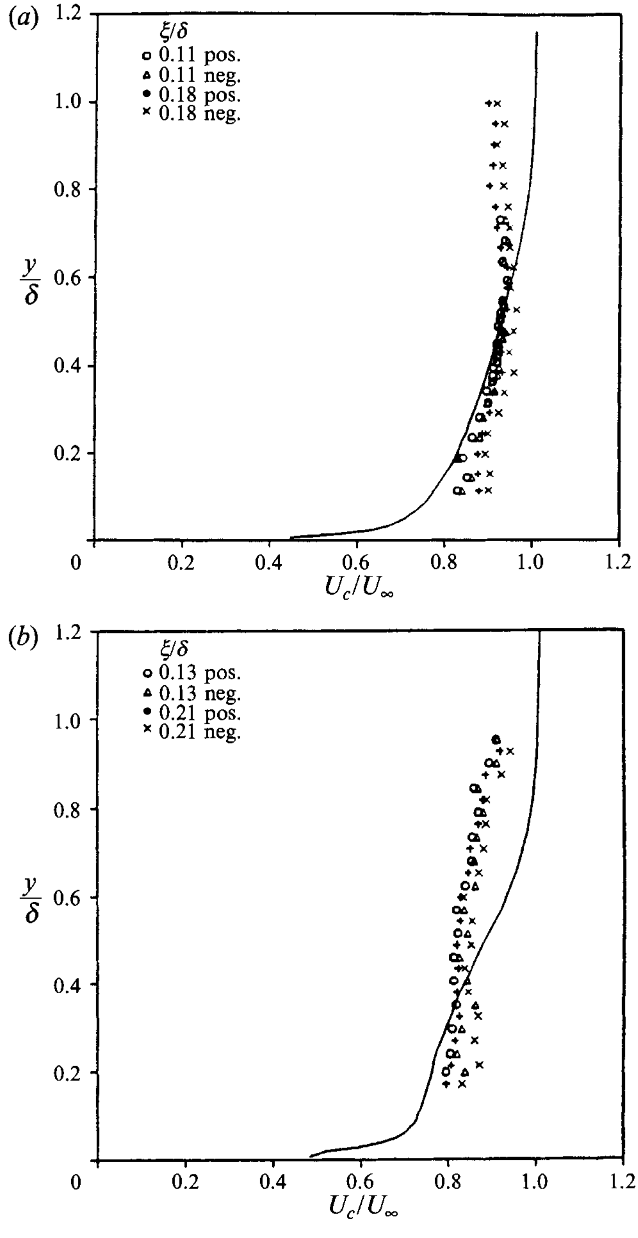

FIGURE 12. Averaged instantaneous convection velocity based upon VITA events (*a*) in the upstream boundary layer, and (*b*) at $x/\delta_0 = 5.4$.

averaging many values removes much of the temporal bias, and the average value of the instantaneous convection velocity is therefore more accurate than measurements of the broadband convection velocity (note that the apparent variation with probe separation seen in figure 11(*b*) is no longer present). Agreement with the broadband convection velocity is good, and the reduced convection velocity is confirmed. In all cases, distributions of the instantaneous convection velocity were found to have small standard deviations: between 0.04 and 0.10 of the free-stream velocity (the distributions downstream of curvature were somewhat broader than in the unperturbed case).

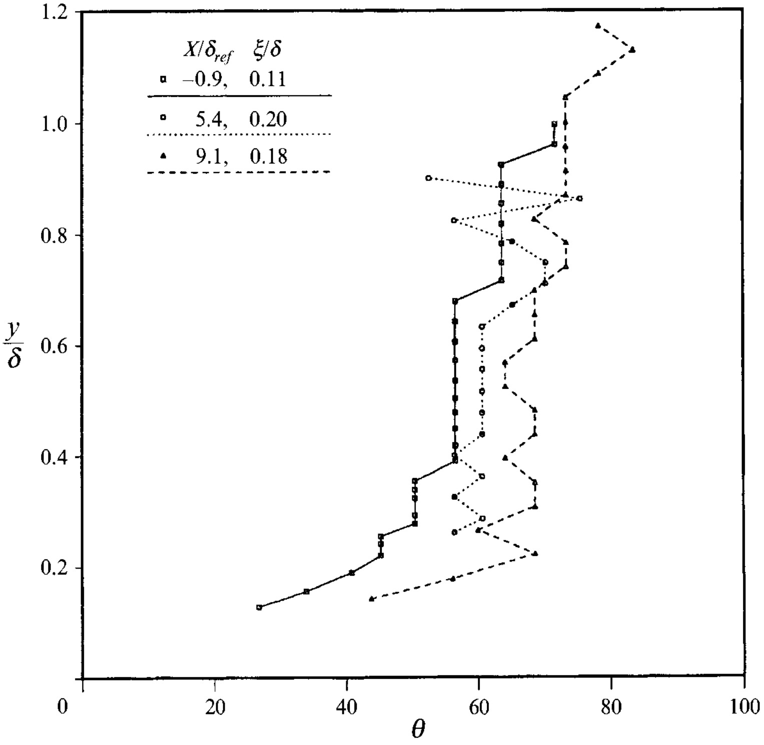

FIGURE 13. Structure angle profiles at three streamwise locations.

Owen & Horstman (1972) argued that the transducer separation should be larger than δ so that the probes do not detect small-scale motions that can change significantly between passing the first and second wires. Conditional sampling avoids that difficulty since it detects only the large-scale motions. Agreement between the average convection velocity of the large-scale motions and the broadband convection velocity indicates that at the wire separations used here the small-scale motions do not significantly affect the time shift of the cross-correlation.

6.2. *Structure angle*

Measurements were also taken with two normal wires separated by a fixed distance in the direction normal to the wall. The time delay corresponding to the peak value of the correlation between the two signals, τ_{max}, is consistently non-zero, indicating that the organized motions in the boundary layer are, on average, inclined at an angle to the wall. This angle, termed the structure angle (Spina & Smits 1987), may be calculated according to:

$$\theta = \tan^{-1}(\xi/U_c\tau_{max}),$$

where ξ is the vertical spacing between the wires. The convection velocity, U_c, was taken to be $0.9U_e$ in the unperturbed layer and $0.85U_e$ downstream of curvature, although the structure angle is relatively insensitive to the choice of convection velocity: for an angle of 45°, a 10% uncertainty in the convection velocity gives an uncertainty in the angle of only 3° for the wire separations used here. Spina *et al.* (1991*a*) showed that the structure angle in the upstream, unperturbed boundary layer is approximately 50° throughout the middle region of the boundary layer and the

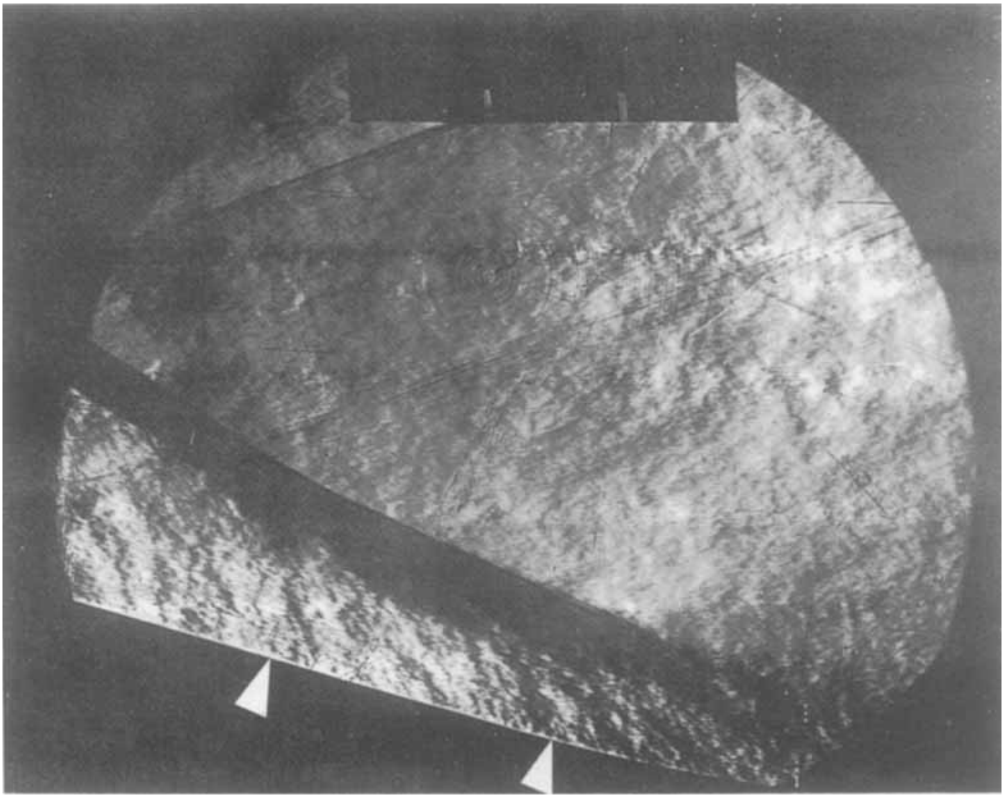

FIGURE 14. Schlieren photograph with the fences removed. The flow is from right to left and the first pointer indicates the end of curvature and the second indicates the $x/\delta_0 = 5.4$ location.

profile is independent of wire separation for $0.1\delta < \xi < 0.4\delta$. Thus, motions in the boundary layer contributing to the cross-correlation are of relatively large vertical extent.

Since this technique relies on the accurate determination of the time delay between the signals of the two hot wires, great care was taken to ensure that the frequency responses of the two wires were as similar as possible. The repeatability of structure angle measurements with the same wire spacing and the good agreement between the distributions measured with different spacings lends confidence to the measurements.

The structure angle profiles are shown in figure 13. The distance from the wall of each data point was taken as the point midway between the two wires. Some of the scatter is due to the limited temporal resolution of the signals: for the smallest wire spacing (0.09δ) an angle of 45° has an uncertainty of 6° (given the sampling rate of 1 Mhz). Despite some scatter, it is clear that the angle increases by approximately 10°.

Schlieren photography was used to visualize the flow with the side fences removed to allow optical access (see figure 14). The edges of the flow-field became significantly three-dimensional: in particular, the shock wave which formed outside the boundary layer wrapped around the model (the shock wave is seen as the dark region above the boundary layer in the recovery region). However, the central portion of the flow remained reasonably two-dimensional. Note that the upstream boundary layer is not visible in figure 14 owing to the location of the optical access window. The density structures in the upstream part of the curved region appear to have a smaller inclination (relative to the local wall orientation) than that observed in the upstream boundary layer (see, e.g. Smith & Smits 1988; Spina *et al.* 1991*a*). By $x = 5.4\delta_0$ the angles appear to have become larger than those observed in the incoming boundary layer. After viewing many schlieren images, the increase in the angle of the density structures was estimated to be about 15° at $x/\delta_0 = 8.9$. A correspondence between the density structures and the structures which comprise the peak of the cross-correlation curve was first noted by Spina *et al.* (1991*a*) for the zero-pressure-gradient boundary layer. This relation now can be extended to perturbed flows since the cross-correlation and schlieren methods both indicate a similar increase in structure angle.

A simple calculation based on the magnitude of the compression in the plane of curvature (assuming the perturbation to be rapid) suggests that the angle should decrease, not increase. If we assume the incoming large-scale motions have a vertical scale given by δ, and the overall streamwise extent is given by $\eta\delta$, then $\eta = 1.1$ for most of the central part of the upstream layer since the structure angle is about 50° (see figure 13). Furthermore, if we assume that the vertical scale downstream is still given by the local boundary-layer thickness, then the downstream value of η can be found from the velocity ratio across the compression, as long as the viscous terms are negligible for this short time. This would imply that the downstream angle is close to 20°, primarily because of the reduction in boundary-layer thickness. If the organized motion were some type of vortical structure, then considerable stretching would be required to rotate it to an angle of 20° and still have it span the boundary layer (this leads to an increase in length of about 90%). If the structure is assumed to be a large-scale horseshoe vortex, then stretching would cause the legs of the vortex to move closer while their circulation remains constant. Using a Biot-Savart-type argument (assuming the gradients of the sound speed are not large in the outer 80% of the boundary layer), the induced velocity will increase, tending to increase the angle of inclination. As noted, the schlieren photographs suggest that the inclination angle of density structures first decreases in the middle of the curved region and then increases beyond the initial values after the curvature is removed (see figure 14), suggesting that an over-recovery of the structure angle occurs in the region after curvature.

In incompressible flows, some investigators (for example, Head & Bandyopadhyay 1981) have discussed the possibility that the angles of inclination of hairpin vortices and bulge interfaces are related to the principal axis of the rate of strain tensor. In any zero-pressure-gradient boundary layer the inclination of the principal axis is very close to 45°. Donovan (1989) used a rotational method of characteristics to calculate the variation of the rate of strain tensor for the current experiment. This procedure is valid for rapidly distorted flows where the turbulence has a negligible effect on the mean flow, a condition satisfied reasonably well by the flow for $x \geqslant 5.4\delta_0$. The smallest inclination of the principal axis was calculated to be about 40° before relaxing back to its upstream value, which to some extent reflects the behaviour observed in the schlieren visualization. However, the causal relation between the principal axis of the mean strain rate and the inclination of the organized motions remains unclear.

The broadband structure angle includes contributions from all of the motions which span a distance larger than the wire spacing. To isolate the angles associated with the individual energetic motions, two-point VITA conditional sampling was again used (in a manner similar to that used to determine individual structure convection velocities). Spina & Smits (1987) found that the standard deviation of the structure angle for both positive and negative events in the unperturbed boundary layer was quite high, approximately 20° across the boundary layer. Owing to this large variation in structure angle, the mean angle may not be a good way to characterize organized motions. However, agreement between the average individual structure angle and the mean structure angle based upon the cross-correlation was within 5° in all cases (exact agreement cannot be expected because of the nonlinear transformation between time shift and structure angle).

6.3. *Space–time correlations for vertically separated wires*

The variation of the peak cross-correlation coefficient in the upstream boundary layer for vertically separated wires was given by Spina *et al.* (1991*a*). The corresponding curves for the downstream boundary layer at $x/\delta_0 = 5.4$ show little difference, and in both cases a correlation level of 0.1 was still observed for a wire separation of 0.5δ, indicating the large vertical extent of the organized motions. A correlation level of 0.1 for a separation of 0.5δ should be considered a relatively high value because the large variation in the instantaneous structure angle tends to smear the cross-correlation, especially for large separations.

While the peak values of the space–time correlation curves were not significantly changed through the curved region, the correlation curves did become broader. The width (in time) of a correlation curve at a specific correlation level gives an indication of the streamwise lengthscales of motions that both wires detect. Cross-correlation curves obtained downstream of the curved region exhibit an increase in this width. While an increase in the standard deviation of the individual structure angles would also broaden the cross-correlation curves, the differences in the angle distributions between the upstream and downstream cases are not sufficient to account for the changes in the curves. Thus an increase in the spatial extent of the organized motions seems to be indicated.

Spatial information is difficult to discern from the cross-correlation curves themselves, but a qualitative picture can be obtained by generating a correlation surface from the individual cross-correlation curves. First, the mean-structure shape based upon the mean structure angle is constructed. At each point that makes up the structure shape the cross-correlation is plotted with its peak value aligned to the structure-shape line. A surface is then fitted through the individual curves and represents the streamwise spatial nature of the large-scale motions that both wires interpret. However, a two-dimensional presentation of these surfaces makes quantitative comparisons difficult, and contour plots of constant correlation coefficient are more useful. Contours for the vertical space–time correlations are shown in figure 15. The plots illustrate the spatial nature of the organized motions in side-view when the x-axis is considered to be the streamwise direction (using Taylor's hypothesis). Contours for the unperturbed boundary layer below 0.5δ and upstream of the peak are inclined at smaller angles than the contours downstream of the peak. This behaviour may mean that organized motions attached to the wall are being stretched considerably by the mean velocity gradient and swept back along the wall. The contours downstream of curvature exhibit the same behaviour, but the difference in angle extends out to the edge of the boundary layer. The increase in mean structure angle is also evident.

While the character of the contours is the same in both cases, the contour levels drop off more quickly in the upstream boundary layer. For example, at $y/\delta = 0.5$ the streamwise length based upon the $R_{ab} = 0.2$ contour increases by a factor of 1.6 owing to the perturbation, which is consistent with the increase of low-frequency energy in the streamwise fluctuating mass flux. This change is much larger than could be accounted for by the corresponding decrease in U_c/δ of 7%, and neither is it consistent with the stretching argument presented earlier, nor with the effects of bulk compression. Alternatively, the apparent increase in the lengthscale could indicate that the primary

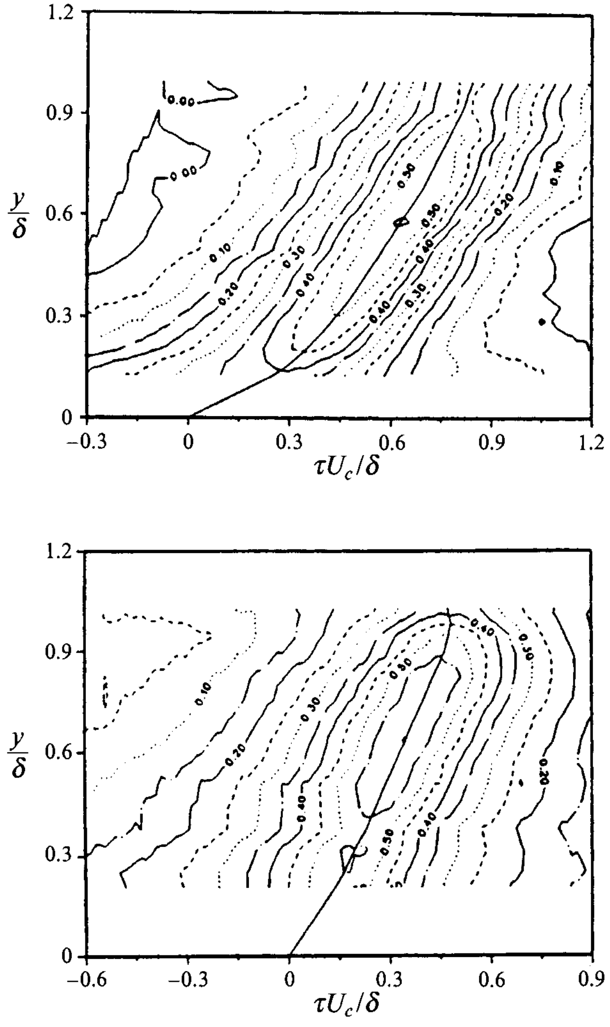

FIGURE 15. Correlation contours from hot wires separated by 0.1δ in a direction normal to the wall for the unperturbed boundary layer (top) and at $x/\delta_0 = 5.4$ downstream of the start of curvature (bottom).

contributors to the correlation have been amplified more than the uncorrelated contributions, even if the timescale of the primary contributions decreased. This would also help to explain the slightly higher peak correlation value seen in the downstream boundary layer.

The vertical extent of the organized motions was determined by varying the wire separation while keeping the midpoint a constant distance from the wall. As in the case of the streamwise extent, the vertical extent increased relative to the boundary-layer thickness: based upon the 0.2 contour, the height increased by a factor of 1.2, supporting the results of the stretching argument.

The frequencies of motions that contribute to the cross-correlations can be determined from the cospectrum (see Donovan 1989 for details). As the spacing is increased, it was found that the area under the curve decreased, reflecting the decrease in peak cross-correlation coefficient. In addition, the contribution from high frequencies was reduced. For example, as the separation was increased from 0.1δ to

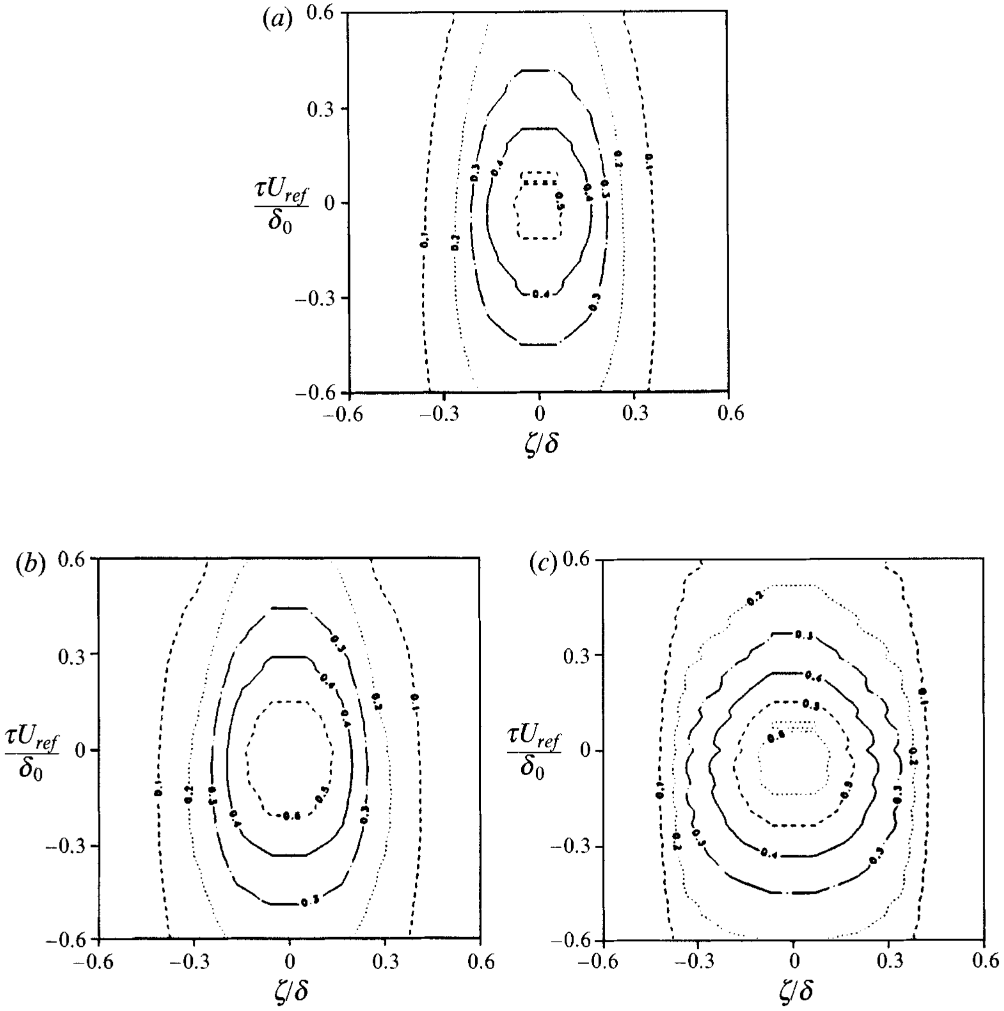

FIGURE 16. Contours of the correlation surface generated using spanwise wire separations at (*a*) 0.2δ, (*b*) 0.5δ, and (*c*) 0.8δ at $x/\delta_0 = 5.4$.

0.6δ, the maximum frequency contributing to the cross-correlation in the upstream boundary layer decreased by almost an order of magnitude. Downstream, the contribution from frequencies below $0.2\delta_0/U_{ref}$ increased, and the contribution from frequencies above this value decreased. A similar effect was observed in the streamwise mass-flux spectra. The increase in low-frequency energy is consistent with the increase in the streamwise extent of the organized motions.

6.4. *Space–time correlations for spanwise-separated wires*

Contour plots of the spanwise space–time correlations, generated in the same manner used to produce figure 15, are shown in figure 16. Since the correlation is symmetric in the wire-separation direction, the contours were reflected about the zero-separation line. To the extent that Taylor's hypothesis holds, these contour plots can be considered as plan views of the average organized motion at different heights in the boundary layer. The upstream and downstream contours are qualitatively similar (see Spina *et al.* 1991*a* for the upstream data) but the spanwise and streamwise extents of the correlation contours increase through the perturbation. From figure 15 we note that in the upstream boundary layer at $y = 0.5\delta$ the correlation contour of 0.2 has a vertical extent of 0.36δ and a streamwise extent of 0.73δ. Downstream, these dimensions increase to 0.43δ and 1.36δ, respectively. The spanwise scale is affected to a much smaller degree: the average spanwise extent is about 0.57δ in the upstream flow and 0.63δ at the downstream station.

7. Flow-field reconstruction

By simultaneously applying conditional sampling to the streamwise fluctuating mass flux and normal fluctuating velocity signals, an approximate view of the flow-field associated with the average large-scale motion can be derived.

Spina *et al.* (1991 *a*) showed that in this supersonic boundary layer strong, positive VITA events correspond to mass-flux 'fronts' which extend over significant fractions of the boundary-layer thickness. This implies that single-point measurements can be used to determine the ensemble-averaged velocity field about a large-scale motion if only strong VITA events are selected. The positive VITA velocity signatures (figure 10) can be interpreted as a cut through the ensemble-averaged velocity field at a single wall-normal location. Streamwise mass-flux gradients are assumed to convect at a constant convection velocity throughout the layer, and this value is $0.9U_e$ in the unperturbed boundary layer and $0.85U_e$ downstream of the curved region. Since the fluctuating quantities used to determine the ensemble-averages are relative to the local mean, the difference between the local mean and the convection velocity is added to the ensemble-averaged velocities at each location to obtain a velocity which would be observed in a reference frame fixed to the mass-flux gradient. Morkovin's (1962) strong Reynolds analogy was used to convert instantaneous streamwise mass flux to instantaneous velocity. The centres of the events are then displaced to correspond to the mean structure shape, as were the isocorrelation contours described in §6.3.

For the upstream boundary layer, the resulting velocity fields are shown in figure 17(*a*). Only positive events, which correspond to the upstream side (back) of a turbulent bulge, are shown. The mean structure shape is also indicated on these plots as determined from the double normal wire measurement discussed earlier. This field is essentially the velocity field seen as if convecting with the mass-flux gradient interface of the ensemble-averaged structure. As discussed by Spina *et al.* (1991 *a*), the velocity vectors shown at the structure shape line have a non-zero streamwise component. The location of the centre of the event determines this velocity and here it is rather arbitrary, being based upon a maximum in the short time variance. The 'edge' of the motion is also rather difficult to define as a line. Nevertheless, this representation appears to capture, qualitatively, the character of the ensemble-averaged flow field.

Similar velocity fields in the downstream flow are shown in figure 17(*b*). The rotating motion of the fluid downstream of the back is not as well defined and the upward velocity just before the mass flux gradient is much larger than in the upstream boundary layer. Fluid upstream of the interface turns away from the wall much sooner in this case as well. Throughout the flow the amplification of the normal velocity is greater than that of the streamwise component, as indicated by the steeper angle of most of the vectors. Clearly, the amplification of u and v is quite different. Note that the results are shown for a single station. The schlieren photographs (and the R_{uv} results) suggest a rapid reorganization of the structure and the resulting flow field will clearly depend on survey location.

The joint probability density distributions of the $\rho u'$ and v' signals confirmed that a

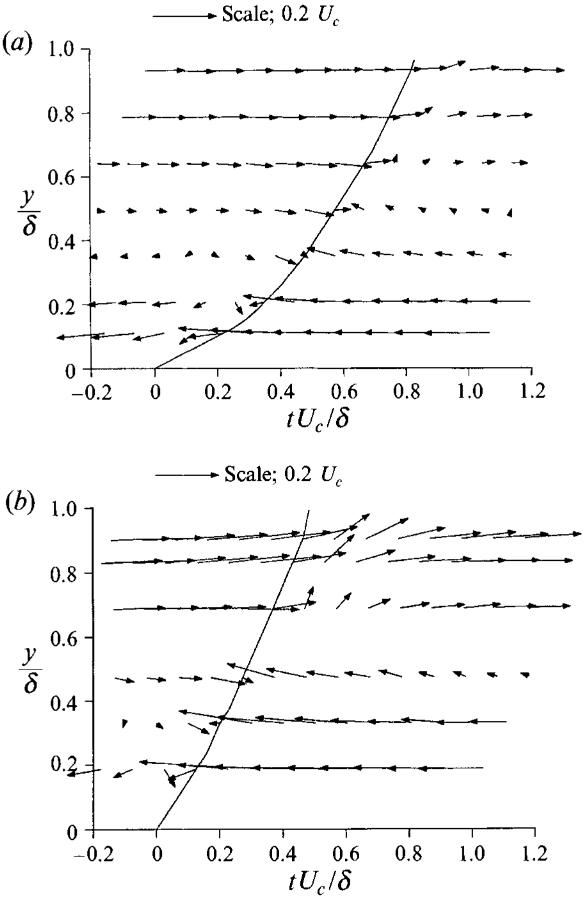

FIGURE 17. Average flow field in the region of the positive mass-flux gradient as seen in a reference frame moving at the convection velocity for (*a*) the upstream boundary layer and (*b*) the boundary layer at $x/\delta_0 = 5.4$.

redistribution occurred throughout the boundary layer. Donovan (1989) studied these distributions, and applied the quadrant conditional sampling technique (Wallace, Eckelmann & Brodky 1972) to the data. The results are most useful when applied to the upstream boundary layer (see Spina *et al.* 1991*a*), and the results in the downstream boundary layer do not add significant insight to what has already been found.

8. Conclusions

We have seen that the Reynolds stresses are strongly amplified by the combined effects of adverse pressure gradient, bulk compression, and concave streamline curvature. When compared to the experiment by Smith (1993) on a flat plate with the same pressure distribution, the additional effect of concave curvature is seen to enhance this amplification considerably (accounting for an additional 60%–70% increase in turbulence levels and skin friction). The Reynolds stress ratios showed some contrasting behaviour: the anisotropy ratio was virtually unchanged, whereas R_{uv} increased by more than 60%. These major changes in the Reynolds-averaged structure parameters were also reflected in more direct measurements of the turbulence structure. For example, the characteristic structure angles increased significantly, reflecting the pronounced increase in v' activity, and lengthscales derived from correlation measurements showed that the streamwise extent of the average large-scale motion nearly doubled, with relatively small increases in the other directions.

Conditional sampling of the streamwise fluctuating mass flux indicated that the signatures of the mass flux gradients are compressed in time somewhat, implying a decrease in lengthscale. As discussed in §6.2, if the motions responsible for the streamwise mass flux gradients were of a vortical nature, then the stretching which occurs owing to the curvature would intensify the gradient region on the upstream side of the low-speed bulge. Thus, the overall lengthscale of the large-scale motions increases while the gradient region is intensified, effectively reducing its length-scale.

By presenting the conditionally sampled ensemble averages in the form of a flow field associated with the large-scale structures, several changes were observed. First, the gradient at the upstream edge of the low-speed region was intensified. After the curved region, flow away from the wall in the outer part of the boundary layer just downstream of the gradient region was intensified. Throughout the sharp gradient region, the angles of the velocity vectors relative to the horizontal were increased in magnitude in the perturbed boundary layer. This result implies a decrease in the anisotropy ratio, $\overline{u'^2}/\overline{v'^2}$, but measurements indicate that the anisotropy ratios in the downstream region are essentially identical to those of the upstream boundary layer.

This work was supported by the Air Force Office of Scientific Research under Grants 88-0120 and 89-0420, monitored by Dr James McMichael.

REFERENCES

ALVING, A. E. 1988 Boundary layer relaxation from convex curvature. PhD thesis, Princeton University.

BLACKWELDER, R. & KAPLAN, R. E. 1976 On the wall structure of the turbulent boundary layer. *J. Fluid Mech.* **76**, 89–112.

BRADSHAW, P. 1973 The effect of streamline curvature on turbulent flow. NATO Advisory Group for Aerospace Research and Development, *AGARDograph* 169.

BRADSHAW, P. & UNSWORTH, K. 1974*a* Comment on evaluation of Preston tube calibration equations in supersonic flow. *AIAA J.* **12**, 1293–1295.

BRADSHAW, P. & UNSWORTH, K. 1974*b* An improved Fortran program for the Bradshaw–Ferris–Atwell method of calculating turbulent shear layers. *Imperial College Aero Rep.* 74-02.

CHOU, J. H. & CHILDS, M. E. 1983 An experimental study of surface curvature effects on a supersonic turbulent boundary layer. *AIAA paper* 83-1672.

CLAUSER, F. H. 1954 Turbulent boundary layers in adverse pressure gradients. *J. Aeronaut. Sci.* **21**, 91–108.

DONOVAN, J. F. & SPINA, E. F. 1992 An improved analysis method for crossed-wire signals obtained in supersonic flow. *Exps Fluids* **12**, 359–368.

DONOVAN, J. F. 1989 The structure of supersonic turbulent boundary layers subjected to concave surface curvature. PhD thesis, Princeton University, Princeton, NJ.

FERNANDO, E. M. 1988 The effects of an adverse pressure gradient on a flat plate supersonic, turbulent boundary layer. PhD thesis, Princeton University, Princeton, NJ.

FERNANDO, E. M. & SMITS, A. J. 1990 A supersonic turbulent boundary layer in an adverse pressure gradient. *J. Fluid Mech.* **211**, 343–362.

FERNHOLZ, H. H. & FINLEY, P. J. 1980 A critical commentary on mean flow data for two-dimensional compressible turbulent boundary layers. NATO Advisory Group for Aerospace Research and Development, *AGARDograph* 253.

FERNHOLZ, H. H., FINLEY, P. J., DUSSAUGE, J. P. & SMITS, A. J. 1989 A survey of measurements and measuring techniques in rapidly distorted compressible turbulent boundary layers. NATO Advisory Group for Aerospace Research and Development, *AGARDograph* 315.

GAVIGLIO, J. 1987 Reynolds analogies and experimental study of heat transfer in the supersonic boundary layer. *Intl J. Heat Mass Transfer* **30**, 911–926.

HAYAKAWA, K., SMITS, A. J. & BOGDONOFF, S. M. 1984 Hot-wire investigation of an unseparated shock-wave/turbulent boundary layer interaction. *AIAA J.* **22**, 579–585.

HEAD, M. R. & BANDYOPADHYAY, P. 1981 New aspects of turbulent boundary layer structure. *J. Fluid Mech.* **107**, 297–338.

HOYDYSH, W. G. & ZAKKAY, V. 1969 An experimental investigation of hypersonic turbulent boundary layers in adverse pressure gradient. *AIAA J.* **7**, 105–116.

JAYARAM, M., TAYLOR, M. W. & SMITS, A. J. 1987 The response of a compressible turbulent boundary layer to short regions of concave surface curvature. *J. Fluid Mech.* **175**, 343–362.

LADERMAN, A. J. 1980 Adverse pressure gradient effects on supersonic boundary layer turbulence. *AIAA J.* **18**, 1186–95.

MCLAFFERTY, G. H. & BARBER, R. E. 1962 The effect of adverse pressure gradient on the characteristics of turbulent boundary layers in supersonic streams. *J. Aero. Sci.* **29**, 1–10.

MORKOVIN, M. V. 1962 Effects of compressibility on turbulent flows. *Intl Symp. on the Mechanics of Turbulence*, CNRS, Paris.

MORKOVIN, M. V. 1992 Mach number effects on free and wall turbulent structures in light of instability flow interactions. In *Studies in Turbulence* (ed. T. B. Gatski, S. Sarkar & C. J. Speziale). Springer.

OWEN, F. K. & HORTSMAN, C. C. 1972 On the structure of hypersonic turbulent boundary layers. *J. Fluid Mech.* **53**, 611.

SETTLES, G. S. & TENG, H. Y. 1982 Flow visualization of separated three-dimensional shock wave/turbulent boundary layer interactions. *AIAA paper* 82-0029.

SMITH, D. R. 1993 The response of a turbulent boundary layer in supersonic flow to successive distortions. PhD thesis, Princeton University.

SMITH, D. R., FERNANDO, E. M., DONOVAN, J. F. & SMITS, A. J. 1992 Conventional skin friction measurement techniques for strongly perturbed supersonic turbulent boundary layers. *Eur. J. Mech* B **11**, 719–740.

SMITH, D. R. & SMITS, A. J. 1993 Direct measurements of the velocity and temperature field in turbulent boundary layers at Mach 3. *Expl Thermal Fluid Sci.* (to appear).

SMITH, M. W. & SMITS, A. J. 1988 Cinematic visualization of coherent density structures in a supersonic turbulent boundary layer. *AIAA paper* 88-0500.

SMITS, A. J., EATON, J. A. & BRADSHAW, P. 1979*a* The response of a turbulent boundary layer to lateral divergence. *J. Fluid Mech.* **94**, 243–268.

SMITS, A. J., HAYAKAWA, K. & MUCK, K. C. 1983 Constant temperature hot-wire anemometry practice in supersonic flows, Part I: the normal wire. *Exps Fluids* **1**, 83.

SMITS, A. J. & MUCK, K. C. 1987 Experimental study of three shock wave turbulent boundary-layer interactions. *J. Fluid Mech.* **182**, 291–314.

SPINA, E. F., DONOVAN, J. F. & SMITS, A. J. 1991*a* On the structure of high-Reynolds-number supersonic turbulent boundary layers. *J. Fluid Mech.* **222**, 293–327.

SPINA, E. F., DONOVAN, J. F. & SMITS, A. J. 1991*b* Convection velocity in supersonic turbulent boundary layers. *Phys. Fluids* A **3**, 3124–3126.

SPINA, E. F. & SMITS, A. J. 1987 Organized structure in a compressible turbulent boundary layer. *J. Fluid Mech.* **182**, 85–109.

STUREK, W. B. & DANBERG, J. E. 1972*a* Supersonic turbulent boundary layer in adverse pressure gradient, Part I: the experiment. *AIAA J.* **10**, 475–480.

STUREK, W. B. & DANBERG, J. E. 1972*b* Supersonic turbulent boundary layer in adverse pressure gradient, Part II: data analysis. *AIAA J.* **10**, 630–635.

THOMANN, H. 1968 Effect of streamwise wall curvature on heat transfer in a turbulent boundary layer. *J. Fluid Mech.* **156**, 419.

VAN DRIEST, E. R. 1951 Turbulent boundary layer in compressible fluids. *J. Aero. Sci.* **128**, 283.

WALLACE, J. M., ECKELMANN, H. & BRODKEY, R. S. 1972 The wall region in turbulent shear flow. *J. Fluid Mech.* **54**, 39.